Published in final edited form as:

Nature. 2021 March ; 591(7849): 293–299. doi:10.1038/s41586-021-03237-4.

Loss of Furin Cleavage Site Attenuates SARS-CoV-2 Pathogenesis

Bryan A. Johnson[1,*], **Xuping Xie**[2,*], **Adam L. Bailey**[5,*], **Birte Kalveram**[3], **Kumari G. Lokugamage**[1], **Antonio Muruato**[1], **Jing Zou**[2], **Xianwen Zhang**[2], **Terry Juelich**[3], **Jennifer K. Smith**[3], **Lihong Zhang**[3], **Nathen Bopp**[3], **Craig Schindewolf**[1], **Michelle Vu**[1], **Abigail Vanderheiden**[5,6,7], **Emma S. Winkler**[5,12], **Daniele Swetnam**[2], **Jessica A. Plante**[1], **Patricia Aguilar**[3], **Kenneth S. Plante**[1], **Vsevolod Popov**[3], **Benhur Lee**[9], **Scott C. Weaver**[1,4], **Mehul S. Suthar**[6,7,8], **Andrew L. Routh**[2], **Ping Ren**[3], **Zhiqiang Ku**[10], **Zhiqiang An**[10], **Kari Debbink**[11], **Michael S. Diamond**[5,12,13], **Pei Yong Shi**[2,4,#], **Alexander N. Freiberg**[3,4,#], **Vineet D. Menachery**[1,4,#]

[1]Department of Microbiology and Immunology, University of Texas Medical Branch, Galveston, TX, USA

[2]Department of Biochemistry and Molecular Biology, University of Texas Medical Branch, Galveston, TX, USA

[3]Department of Pathology, University of Texas Medical Branch, Galveston, TX, USA

[4]Department of Institute for Human Infection and Immunity, University of Texas Medical Branch, Galveston, TX, USA

[5]Department of Pathology & Immunology, Washington University School of Medicine, St. Louis, MO, USA

[6]Department of Pediatrics, Emory University School of Medicine, Atlanta, GA, USA.

[7]Emory Vaccine Center, Emory University School of Medicine, Atlanta, GA, USA.

[8]Yerkes National Primate Research Center, Atlanta, GA, USA

Corresponding Author: Vineet D. Menachery, **Address:** University of Texas Medical Branch, 301 University Blvd, Route #0610 Galveston, TX 77555, Vimenach@utmb.edu.

*Equal contributions

#Co-senior authors

Author Contributions

Conceptualization, XX, BAJ, ALR, MS, ANF, P-YS, and VDM; Methodology, BAJ, XX, BK, KGL, DS, ALR, ANF, P-YS and VDM.; Investigation, BAJ, XX, BK, KGL, AM, JZ, XZ, TJ, JKS, LZ, CS, MV, AV, ESW, DS, NB, JAP, ALR, KD, and VDM.; Resources, KSP, SCW, MSS, PR, VP, ZK, ZA, P-YS, MSD. ANF, VDM; Data Curation, BAJ, XX, BK, KGL, AV, ESW, DS, ALR, MSS, KD, P-YS, ANF, VDM.; Writing-Original Draft, VDM; Writing-Review & Editing, BAJ, XX, BL, PA, MSS, KD, VP, ZK, ZA, P-YS, ANF, VDM, MSD, P-YS; Data Visualization, XX, BAJ, ALB, BK, KGL, NB, ANF, VDM; Supervision, PA, SCW, MSS, P-YS, ANF, VDM.; Funding Acquisition, PA, SCW, P-YS, ANF, VDM.

Competing interests

XX, P-YS, and VDM have filed a patent on the reverse genetic system and reporter SARS-CoV-2. Other authors declare no competing interests. M.S.D. is a consultant for Inbios, Vir Biotechnology, NGM Biopharmaceuticals, and on the Scientific Advisory Board of Moderna and Immunome. The Diamond laboratory has received unrelated funding support in sponsored research agreements from Moderna, Vir Biotechnology, and Emergent BioSolutions.

Additional Information

Supplementary Information is available for this paper. Correspondence and requests for materials should be addressed to P-YS, ANF or VDM.

[9]Icahn School of Medicine at Mount Sinai, New York, NY, USA

[10]Texas Therapeutics Institute, Brown Foundation Institute of Molecular Medicine, University of Texas Health Science Center at Houston, Houston, USA.

[11]Bowie State University, Bowie, MD, USA

[12]Department of Medicine, Washington University School of Medicine, St. Louis, MO, USA

[13]Department of Molecular Microbiology, Washington University School of Medicine, St. Louis, MO, USA

Abstract

SARS-CoV-2, a novel coronavirus (CoV) producing worldwide pandemic[1], has a furin cleavage site (PRRAR) in its spike protein that is absent in other group 2B CoVs [2]. To explore whether the furin cleavage site contributes to infection and pathogenesis, we generated a mutant SARS-CoV-2 deleting the furin cleavage site (ΔPRRA). SARS-CoV-2 ΔPRRA replicates with faster kinetics, has improved fitness in Vero E6 cells, and has reduced spike protein processing as compared to parental SARS-CoV-2. However, the ΔPRRA mutant has reduced replication in a human respiratory cell line and was attenuated in both hamster and K18-hACE2 transgenic mouse models of SARS-CoV-2 pathogenesis. Despite reduced disease, the ΔPRRA mutant conferred protection against rechallenge with the parental SARS-CoV-2. Importantly, COVID-19 patient sera and receptor-binding domain (RBD) monoclonal antibodies had lower neutralization values against the ΔPRRA mutant versus parental SARS-CoV-2 likely due to increased particle/PFU ratio. Together, these results demonstrate a critical role for the furin cleavage site in SARS-CoV-2 infection and highlight the importance of this site in evaluating antibody neutralization activity.

Keywords

Coronavirus; 2019-nCoV; SARS-CoV-2; COVID-19; furin-cleavage; spike

The emergence of severe acute respiratory syndrome coronavirus 2 (SARS-CoV-2) has ushered in a worldwide pandemic [1,3]. The novel coronavirus, like severe acute respiratory syndrome (SARS)-CoV and Middle East Respiratory Syndrome (MERS)-CoV, induces severe respiratory disease including fever, multi-lobar pneumonia, and in many cases, death [4]. While SARS-CoV-2 shares a similar genomic structure and protein homology with SARS-CoV, its ability to spread asymptomatically and cause mild to severe disease distinguishes it from the earlier pandemic CoV [5]. Examining the spike (S) protein, a glycoprotein responsible for receptor binding and entry following cleavage at its S1/S2 and S2 sites (Extended Data Fig. 1a), studies indicate that SARS-CoV-2 has greater affinity for the ACE2 receptor than SARS-CoV [6]. Notably, attention has focused on a furin cleavage motif at the S1/S2 cleavage site [2]. Absent in other group 2B CoVs, the four amino acids (PRRA) form a RXXR cleavage motif for serine proteases when added to S1/S2 cleavage site (PRRAR, Extended Data Fig. 1b) [7]. Structural analysis has shown that furin cleavage facilitates a higher proportion of spike to bind human ACE2 receptor [8] and may have facilitated the emergence of SARS-CoV-2 in humans. To date, the furin cleavage site has been analyzed using mutated pseudotyped viruses that ablate the spike's ability to mediate cell-cell and

virus-cell fusion in Calu-3 cells[9,10]. Other studies have isolated deletion variants of SARS-CoV-2 that span the furin cleavage and S1/S2 site attenuating infection [11,12]. To date, no studies have evaluated the function of the furin site using authentic SARS-CoV-2 containing a precise PRRA deletion. Such studies are necessary as discrepant results reported for the spike D614G mutation highlight differences between pseudotyped and authentic SARS-CoV-2 variants [13,14].

Here, we utilized a reverse genetic system to generate a SARS-CoV-2 mutant lacking the spike furin cleavage site (ΔPRRA) [15]. The PRRA deletion reduced spike protein cleavage, but augmented viral replication in Vero E6 cells. Ectopic expression of TMPRSS2 in Vero E6 cells removed the fitness advantage for ΔPRRA. In contrast, the ΔPRRA mutant was attenuated in a human respiratory cell line and had reduced viral pathogenesis in both hamsters and K18-hACE2 expressing mice. Notably, the ΔPRRA mutation required more antisera and monoclonal antibodies targeting the receptor-binding domain (RBD) for neutralization. Our results demonstrate a critical role of the furin cleavage site in SARS-CoV-2 infection and highlight the concerns when using the furin deletion variants for COVID-19 research.

Generation of the ΔPRRA mutant.

We generated a mutant virus lacking the PRRA motif using a SARS-CoV-2 reverse genetic system (Fig. 1a) [15]. The furin cleavage site resides in an exterior and ostensibly unresolved loop of the SARS-CoV-2 spike structure below the globular head and away from the RBD (Fig. 1b). We used homology modeling to visualize the PRRA site in this extended loop (cyan). Deletion of the PRRA motif is predicted to shorten the loop without disrupting the overall structure of the spike. Following electroporation, we recovered ΔPRRA mutant SARS-CoV-2 with a titer equivalent to the wild-type (WT) virus. Unexpectedly, the ΔPRRA virus produced a larger plaque size on Vero E6 cells than WT virus, suggesting changes in viral replication and spread in the absence of the furin cleavage site (Extended Data Fig. 1c).

Distinct ΔPRRA replication and cleavage.

To evaluate viral replication, we inoculated Vero E6 cells with WT and ΔPRRA SARS-CoV-2. SARS-CoV-2 replicates robustly in Vero E6 cells, which often are used for virus stock propagation and inactivated vaccine production [16]. Following a low multiplicity of infection (MOI of 0.01 plaque forming units (PFU)/cell), both WT and ΔPRRA viruses replicated to similar end-point titers. However, ΔPRRA mutant had a 25-fold higher viral titer and more cytopathic effect (CPE) at 24 hours post infection (HPI) (Fig. 1c). Thus, the loss of the furin cleavage site augments SARS-CoV-2 replication in Vero E6 cells.

We next evaluated spike processing of the ΔPRRA mutant relative to WT SARS-CoV-2 and SARS-CoV. Vero E6 cells were inoculated at an MOI of ~0.1 for 24 h, and virons purified virions were isolated using sucrose cushion ultracentrifugation. The pelleted virus was examined for spike processing and nucleocapsid (N) protein by western blotting. Following SARS-CoV infection, the majority of the spike protein is in its full-length form (98.6%) (Fig. 1d, Extended Data Fig. 2a, uncropped images in Supplementary Fig. 1 & 2), consistent

with minimal processing. In contrast, the WT SARS-CoV-2 virions had significant spike protein cleavage, with 59.6% cleaved to S1/S2 products. The ΔPRRA mutant reduced the S1/S2 cleavage amount to 14.5%. Given the similar levels of N protein, these results illustrate the differences between SARS-CoV and SARS-CoV-2, and show that SARS-CoV-2 processing of the spike is driven by the furin cleavage site.

Given the replication advantage at 24 HPI (Fig. 1d), we evaluated the fitness of the ΔPRRA mutant relative to WT SARS-CoV-2 in a competition assay. Using PFU to determine the input, we mixed the WT and mutant at different ratios in Vero E6 cells, and used RT-qPCR to quantify relative fitness 24 HPI (Fig. 1e, Extended Data Fig. 2b-c). At a 50:50 ratio, the ΔPRRA mutant outcompeted WT virus becoming nearly 90% of the viral population at 24h. A 90:10 WT-to-mutant input ratio resulted in the ΔPRRA mutant comprising ~65% of the viral sequences at 24h. The inverse 10:90 WT-to-mutant input ratio produced 97% ΔPRRA, further confirming the advantage mutant in Vero E6 cells. The RT-qPCR results were corroborated with deep sequencing analysis (Extended Data Fig. 2d). Thus, deletion of the furin cleavage site provides a fitness advantage in Vero E6 cells, and may contribute to mutations found in WT SARS-CoV-2 cultured on Vero E6 cells.

Attenuation of ΔPRRA in Calu3 cells.

We next evaluated the ΔPRRA mutant in Calu3 2B4 cells, a human lung adenocarcinoma cell line commonly used to study influenza virus and other CoVs [17]. In contrast to Vero E6 cells, the ΔPRRA virus replicated less efficiently than WT (Fig. 1f). At both 48 and 72 HPI, the ΔPRRA mutant had ~10-fold reductions in viral titer indicating the loss of the furin cleavage site impairs viral replication in Calu3. Next, we evaluated spike processing on virions that were produced from Calu3 2B4 cells. Consistent with Vero E6 cells, spike from SARS-CoV was not cleaved to S1/S2. However, ~87.3% of spike from WT SARS-CoV-2 was processed to S1/S2, greater than the 59.6% observed in Vero E6 cells (Fig. 1g, Extended Data Fig. 2e, uncropped images in Supplementary Fig. 1 & 2). Unexpectedly, the ΔPRRA mutant also showed an increase in the S1/S2 cleavage product. This band represented more than twice as much S1/S2 cleavage product (33.1% vs 14.5%) as seen in Vero E6 cell supernatants, although the deletion does result in a major shift from cleaved to uncleaved S protein. While more full-length spike is observed in the WT virus infection, the Calu3 results indicate that even without the furin cleavage site, there is significant processing of the SARS-CoV-2 spike. Thus, factors outside the PRRA motif contribute to cleavage of the SARS-CoV-2 spike in a cell type-dependent manner.

TMPRSS2 reduces ΔPRRA fitness advantage.

One distinction between Vero E6 and Calu3 cells is the expression of host serine proteases like TMPRSS2 18. To determine whether this cell surface protease modulates replication of ΔPRRA, we evaluated infection in Vero cells ectopically expressing *TMPRSS2.* Following low MOI (0.01) infection, both WT and ΔPRRA SARS-CoV-2 replicated to similar levels (Fig. 1h). Next, we performed competition assay to evaluate the fitness of ΔPRRA mutant in the TMPRSS2-Vero E6 cells. With a 50:50 input ratio, the ΔPRRA mutant and WT virus retained equal levels in the TMPRSS2-Vero E6 cells (Fig. 1i). These results demonstrate that

expression of TMPRSS2 reduced the Vero E6 replication/fitness advantage of the ΔPRRA mutant over WT SARS-CoV-2. To examine whether TMPRSS2 affects spike cleavage, we purified virions from TMPRSS2-Vero E6 cells and quantified the full-length to S1/S2 spike ratios (Fig. 1j, uncropped images in Supplementary Fig. 3 & 4). Compared with Vero E6 result, the expression of TMPRSS2 had minimal effect on spike processing ratios (compare Extended Data Fig. 2a,f). Both SARS-CoV and ΔPRRA had mostly full-length form of spike intact (96.4% and 95.9%), whereas WT SARS-CoV-2 had nearly half of the spike processed to S1/S2 form (Extended Data Fig. 2f). Overall, the results argue that (i) TMPRSS2 affects virus entry rather than virion release and (ii) TMPRSS2-Vero cells reduces selection of ΔPRRA mutants.

In vivo attenuation of ΔPRRA mutant.

We next evaluated ΔPRRA mutant *in vivo* using the hamster model of SARS-CoV-2 pathogenesis [19] using four male hamsters challenged via intranasal (i.n.) inoculation with 10^5 PFU of WT SARS-CoV-2 or ΔPRRA mutant (Fig. 2a). Following infection with WT SARS-CoV-2, hamsters steadily lost weight starting at day 2 and continuing through day 8 with peak weight loss nearing 15% (Fig. 2b, Extended Data Fig. 3a). Disease scores peaked at day 8, when animals had ruffled fur, hunched posture, and reduced activity requiring additional monitoring (Fig. 2c, Extended Data Fig. 3b). Despite severe disease, the WT-infected hamsters recovered and regained their starting weight by day 15 (Extended Data Fig. 3a). In contrast, hamsters infected with SARS-CoV-2 ΔPRRA showed minimal weight loss and no disease (Fig. 2b, Extended Data Fig. 3a-b). Hamsters in both infection groups gained weight after day 10, over the remainder of the 28-day time course (Extended Data Fig. 3a). In nasal washes, both WT and ΔPRRA infected hamsters had similar viral titers at 2 DPI (Fig. 2d). However, greater ΔPRRA replication was observed at 3 and 4 DPI relative to the WT SARS-CoV-2. In addition, the WT virus was cleared from the nasal washes a day earlier than the ΔPRRA mutant, although no infectious virus was detected after day 7 in either of the hamster groups. For viral RNA from oral swabs, we observed a similar pattern with higher viral RNA concentrations at 3 and 4 DPI in the ΔPRRA mutant relative to WT (Fig. 2e). However, the viral RNA in the swabs stayed positive though 7 DPI with higher concentrations from the WT than ΔPRRA infected animals. Together, these results suggest that despite attenuated disease, the ΔPRRA mutant replicates efficiently in the oral and nasal cavity of hamsters

Infection with ΔPRRA mutant protects from SARS-CoV-2 rechallenge.

With vaccine strategies that mutate the furin cleavage site [20,21], we evaluated if infection with ΔPRRA protects from SARS-CoV-2 rechallenge. Hamsters previously infected with WT or the ΔPRRA mutant were rechallenged with 10^5 PFU of WT SARS-CoV-2 at 28 days post primary. Both WT and ΔPRRA infected hamsters were protected from weight loss following rechallenge (Fig. 2f and Extended Data Fig. 3b). However, mild disease (ruffled fur) was observed in one animal previously infected with WT SARS-CoV-2 (Extended Data Fig. 3c). In contrast, ΔPRRA mutant-infected hamsters produced neither weight loss nor disease. Nasal wash titers and viral RNA from oral swabs were significantly reduced compared to initial infection in both groups and infectious virus cleared by 4 DPI (Fig. 2g-

h). Primary infection with both ΔPRRA and WT SARS-CoV-2 produced neutralizing antibodies in serum (~1/600 each at day 28) (Fig. 2i) and subsequent rechallenge boosted this activity, though we noted a 2-fold differences in final PRNT50 values with WT versus the ΔPRRA (~1/2000 vs ~1/1000). Together, the results indicate the attenuated ΔPRRA infection induces sufficient immunity to protect hamsters from SARS-CoV-2 rechallenge.

ΔPRRA causes attenuated lung disease in K18-hACE transgenic mice.

To further evaluate pathogenesis, we infected transgenic C57BL/6 mice expressing hACE2 and are permissive for SARS-CoV-2 infection[22]. Male and female K18-hACE2 mice were inoculated via *i.n.* route with 10^3 PFU of WT or ΔPRRA SARS-CoV-2 (Fig. 3a). K18-hACE2 mice infected with WT SARS-CoV-2 lost significantly more weight than ΔPRRA infected mice starting at 4 DPI and continuing through the end of the experiment (Fig. 3b). Attenuated disease corresponded to reduced viral replication at day 2 in the lung, nasal turbinates, and nasal washes (Fig. 3c-e). Significant differences in viral burden, however, were not observed in lungs or brain at 7 DPI (Fig. 3f). To examine changes to the functional properties of the lung, we mechanically ventilated mice via tracheostomy and measured several respiratory biophysical parameters. K18-hACE2 mice infected with WT SARS-CoV-2 had reduced inspiratory capacity (Fig. 3g), a downward deflection in pressure/volume loop (Fig. 3h), and increased tissue dampening, respiratory resistance, and tissue elastance consistent with restrictive lung disease localized to the alveoli and tissue parenchyma (Extended Data Fig. 4a-d). In contrast, only mild changes in pulmonary mechanics were observed in ΔPRRA mutant infected mice. Histopathology of lungs at 7 DPI revealed greater immune cell infiltrates and more extensive tissue damage in mice infected with WT virus (Fig. 3i-j, Extended Data Fig. 4e) than ΔPRRA virus (Fig. 3k). Finally, inflammatory mediators 7 DPI revealed greater induction of a subset of cytokines and chemokines following WT compared to ΔPRRA infection (Fig. 3l, Extended Data Fig. 4f). Chemokines associated with macrophage/monocyte activation including MCP-1, MIP-1β, IP-10, and MIG were greater in WT than ΔPRRA infected mice (Fig. 3l). Several other cytokines and chemokines were increased relative to mock infected animals for both WT and ΔPRRA, but trended higher in WT-infected animals (Extended Data Fig. 4f). Together, the data indicates that the ΔPRRA mutant produces reduced disease and replication at early times following SARS-CoV-2 infection.

Acessing antibody neutralization titers for ΔPRRA.

We next evaluated furin cleavage site deletion on virus neutralization. To quantitate neutralization, we generated a ΔPRRA mutant containing a mNeonGreen (mNG) reporter in open reading frame (ORF)7 and compared results to the WT SARS-CoV-2 [23] (Fig. 4a). Examining seventeen COVID-19 human sera, we found nearly uniform reduction in $PRNT_{50}$ values against the ΔPRRA mutant versus WT (Fig. 4b). The lower $PRNT_{50}$ values were observed in COVID19 serum samples with low, intermediate, or high neutralizing activity (Fig. 4C-E) and averaged a 2.3-fold reduction across the 17 human sera tested. The differences between WT and ΔPRRA were significant for the high and intermediate responders, but below threshold for the low responders due to incomplete neutralization (Extended Data Table 1). The consistency in the reduction may be due to: (a) The spike

proteins has an altered conformation in the ΔPRRA virions, restricting access to more cryptic sites on the spike and allowing WT virus to be more readily neutralized by non-RBD antibodies; (b) more intact spike molecules on the virion surface of ΔPRRA virions, requiring more antibodies to neutralize mutant than WT 2. To explore these possibilities, we evaluated neutralization of the ΔPRRA mutant by three mAbs targeting the SARS-CoV-2 RBD (Fig. 4f-h). Each mAb targets a different site in the RBD, but showed similar reductions in neutralization between WT and ΔPRRA. Whereas the results with mAb1 and mAb3 reached significance, low neutralization levels precluded such conclusions with mAb2 (Extended Data Table 1). Altogether, these results highlight differences in antibody neutralization profiles between the WT and ΔPRRA SARS-CoV-2 mutants.

Differences in the PRNT50 values suggest potential physical variation between WT and ΔPRRA virions. One possible explanation is that the ΔPRRA mutant has more full-length spike protein than WT SARS-CoV-2 (Fig. 1d, Extended Data Fig. 2a), which require more antibody for neutralization. To explore this idea, we examined the WT and ΔPRRA mutant virion by transmission electron microscopy (TEM). We evaluated 40 TEM fields of virions from WT and ΔPRRA stocks for morphology and to determine the particle to PFU ratio. Consistent with previous reports, WT SARS-CoV-2 had classic morphology, forming single virions, and had a particle/PFU ratio approaching 20 (Extended Data Fig. 5, Fig. 4i,). In contrast, the ΔPRRA mutant stocks showed a particle/PFU ratio approaching 80, and nearly 33% of the particles clustered in group >3 virions (Fig. 4j). The results suggest that the ΔPRRA mutant form clusters of viruses reminiscent of norovirus and HCV cloaked virions [24,25], though the mechanism for SARS-CoV-2 clumping remains unclear. Controlling for clumps as single PFU, the particle/PFU ratio drops to approximately 60:1 and is more consistent with the 2- to 3-fold increase in serum required for neutralization. Combined with the increased expression of full-length spike, the clumping results and particle/PFU ratio provide multiple explanations for why the antibody concentrations required for neutralization are higher.

Overall, the loss of the furin cleavage site in the SARS-CoV-2 spike has a major impact on infection and pathogenesis with reduced replication in Calu3 respiratory cells and ablated disease in two SARS-CoV-2 pathogenesis models. These results are consistent with other studies examining in the furin cleavage site[11,12]. However, despite the attenuated disease, the ΔPRRA mutant has some replication advantages over WT SARS-CoV-2, which may lead to cell culture adaptions, possibly complicating results. The ΔPRRA mutant fitness advantage in Vero E6 cell is consistent with reports of furin cleavage site deletions in SARS-CoV-2 preparations and patient samples [11,12]. This issue also has implications for manufacturing inactivated COVID19 vaccine on Vero cells [26]. Similarly, the shift in antibody neutralization of the ΔPRRA virus indicates the possibility of imprecise results [27]. With potential vaccine and therapeutics decisions resting on neutralization values, accuracy is an important issue.

A number of approaches can prevent the emergence of the ΔPRRA mutation in SARS-CoV-2 stocks. In our studies, we found no evidence for ΔPRRA deletion in infectious clone derived WT SARS-CoV-2 through passage 2. By utilizing low passage stocks, the incorporation of this mutation was limited. One alternative uses Vero E6 cell expressing TMPRSS2 to remove the fitness advantage of the ΔPRRA mutant allowing virus

propagation without altering the full-length to S1/S2 processing ratio of its spike protein. However, continued passage risks this or other tissue culture adaptations, and careful monitoring of stock composition is needed. Using plaque purification techniques, WT SARS-CoV-2 can be selected for by its smaller plaque morphology.

The furin cleavage site promotes increased spike cleavage in SARS-CoV-2 that has implications for pathogenesis. As such, vaccines and therapeutics that target the furin cleavage site offer an attractive approach to disrupt COVID-19 infection[20] and could have implications for other CoVs with furin cleavages sites including HKU1-CoV, OC43-CoV, and MERS-CoV. Disruption or improvement of these furin sites could change the trajectory of disease caused by these CoV. In our studies, the ΔPRRA mutant attenuates disease *in vivo* and confers protection from subsequent rechallenge. However, ΔPRRA replication was not ablated, and substantial tissue damage was observed in both *in vivo* pathogenesis models. Importantly, differences in the PRNT50 values suggest potential antigenic differences between WT and the ΔPRRA mutant that could impact vaccination approaches. Strategies that disrupt or ablate the furin cleavage site might result in altered adaptive immune responses if the mutations occurred in dominant epitopes. For example, based on structural studies, loss of the furin site could reduce access to the more open form of the spike necessary to interact with hACE2 receptor and alter the targets for antibody generation[8]. While the attenuation of the ΔPRRA mutant holds promise vaccine development, further studies are needed to fully explore the extent of antibody and cell-based immunity induced by this mutant.

Overall, our data illustrate the critical role that the furin cleavage site has in SARS-CoV-2 infection and pathogenesis. In its absence, the mutant ΔPRRA virus is attenuated in its ability to replicate in certain cell types and cause disease *in vivo*. However, the results are complicated by augmented replication and fitness in Vero E6 cells driven by the absence of TMPRSS2 expression. Similarly, altered antibody neutralization profiles indicate a critical need to survey this mutation in analysis of SARS-CoV-2 treatments and vaccines. Overall, the work highlights the critical nature of the furin cleavage site in understanding spike protein biology and SARS-CoV-2 infection and pathogenesis.

Methods

Viruses and cells.

The recombinant wild-type and mutant SARS-CoV-2 are based on the sequence of USA-WA1/2020 isolate provided by the World Reference Center for Emerging Viruses and Arboviruses (WRCEVA) and was originally obtained from the USA Centers for Disease Control and Prevention as described [16]. Wild-type and mutant SARS-CoV-2 as well as recombinant mouse-adapted recombinant SARS-CoV [28] were titrated and propagated on Vero E6 cells or Vero E6 cells expressing TMPRSS2 (Sekisui XenoTech, Kansas City, KS), grown in DMEM with 5% fetal bovine serum and 1% antibiotic/antimytotic (Gibco). Calu3 2B4 cells were grown in DMEM with 10% defined fetal bovine serum, 1% sodium pyruvate (Gibco), and 1% antibiotic/antimitotic (Gibco). Standard plaque assays were used for SARS-CoV and SARS-CoV-2 [29,30]. All experiments involving infectious virus were conducted at the University of Texas Medical Branch (Galveston, TX), Emory University (Atlanta,

Georgia), or Washington University (St. Louis, Missouri) in approved biosafety level 3 (BSL) laboratories with routine medical monitoring of staff.

Construction of ΔPRRA mutant viruses.

Both wild-type and mutant viruses were derived from the SARS-CoV-2 USA-WA1/2020 infectious clone as previously described [15]. For ΔPRRA construction, the mutation was introduced into a subclone puc57-CoV2-F6 by using overlap PCR with primers ΔPRRA-F (5′-GACTAATTCTCGTAGTGTAGCTAGTCAATCCATC-3′) and ΔPRRA-R (5′-GACTAGCTACACTACGAGAATTAGTCTGAGTC-3′). The resulted plasmid was validated by restriction enzyme digestion and Sanger sequencing. Thereafter, plasmids containing wild-type and mutant SARS-CoV-2 genome fragments were amplified and digested by restriction enzyme. The SARS-CoV-2 genome fragments were purified and ligated *in vitro* to assemble the full-length cDNA according to the procedures described previously[15]. *In vitro* transcription reactions then were preformed to synthesize full-length genomic RNA. To recover the viruses, the RNA transcripts were electroporated into Vero E6 cells. The medium from electroporated cells as harvested at 40 HPI and served as seed stocks for subsequent experiments. Viral mutants were confirmed by sequence analysis prior to use. Synthetic construction of SARS-CoV-2 ΔPRRA mutant was approved by the University of Texas Medical Branch Institutional Biosafety Committee.

In vitro infection.

Viral infections in Vero E6 and Calu3 2B4 cells were performed as previously described [31,32]. Briefly, cells were washed with PBS and inoculated with SARS-CoV or SARS-CoV-2 at a multiplicity of infection (MOI) 0.01 for 60 min at 37 °C. Following inoculation, cells were washed, and fresh media was added to signify time 0. Three or more biological replicates were harvested at each described time. No blinding was used in any sample collections, nor were samples randomized. Microsoft Excel for Mac 2011 was used to analyze data.

Virion purification and Western blotting.

Vero E6 or Calu3–2B4 cells were infected with WT or PRRA mutant viruses at an MOI of 0.01. At 24 or 48 HPI, the culture medium was collected and clarified by low speed centrifugation. Virus particles in the supernatant were subsequently pelleted by ultracentrifugation through a 20% sucrose cushion at 26,000 rpm for 3 h using a Beckman SW28 rotor. Protein lysates were prepared from the pellets using 2X Laemmli Sample buffer (Cat# 161–073, BioRad, Hersules,Ca). Relative viral protein levels were determined by SDS-PAGE followed by Western blot analysis as previously described [16,33]. Briefly, sucrose purified SARS-CoV, SARS-CoV-2, and SARS-CoV-2 ΔPRRA inactivated by boiling in Laemelli Buffer. Samples were loaded in equal volumes into 4–20% Mini-PROTEAN TGX Gels (Biorad# 4561093) and electrophoresed by SDS-PAGE. Protein was transferred to polyvinylidene difluoride (PVDF) membranes. Membranes were blotted with SARS-CoV Spike (S) specific antibodies (Novus Biologicals #NB100–56578), followed by probing with horseradish peroxidase (HRP)-conjugated anti-rabbit antibody (Cell Signaling Technology #7074S). Blots were stripped and re-probed with SARS-CoV Nucleocapsid (N) specific antibodies (provided as a kind gift from Dr. Shinji Makino) and the HRP-conjugated anti-

rabbit secondary IgG. In both cases, signal was developed by treating membranes with Clarity Western ECL substrate (Bio-Rad #1705060) imaging on a ChemiDoc MP System (Bio-Rad #12003154). Densitometry was performed using ImageLab 6.0.1 (Bio-Rad #12012931).

Competition assay and Real-Time PCR.

For competition assays, ratios (50:50, 90:10, 10:90 WT/ΔPRRA) were determined by PFU derived from viral stocks. Vero cells were infected at MOI 0.1 (WT+ ΔPRRA) as described above. RNA from cell lysates were collected using Trizol reagent (Invitrogen). RNA was then extracted from Triazol using the Direct-zol RNA Miniprep Plus kit (Zymo Research #R2072) per the manufacturer's instruction. Extracted RNA was then converted to cDNA with the iScript cDNA Synthesis kit (BioRad #1708891). Quantitative real time PCR (qRT-PCR) was performed with the Luna Universal qPCR Master Mix (New England Biolabs #M3003) on a CFX Connect instrument (BioRad #1855200). For differentiation between wild type SARS-CoV-2 and SARS-CoV-2 ΔPRRA genomes in competition experiments, Primer 1 (Forward - AAT GTT TTT CAA ACA CGT GCA G and Primer 2 (Reverse - TAC ACT ACG TGC CCG CCG AGG) were used to detect wild type genomes only. For detecting total genomes, Primer 1 and Primer 3 (Reverse - GAA TTT TCT GCA CCA AGT GAC A) were used. 8-point standard curves (1×10^1 to 1×10^8 copies/μL) were utilized to quantify the signal. A primer annealing temperature of 63°C was used for all assays.

For detection of viral RNA the nasal washes and oral swabs of SARS-CoV-2 and SARS-CoV-2 ΔPRRA infected hamsters, RNA extraction, cDNA synthesis, and qRT-PCR were performed as described above. For qRT-PCR, Primer 1 and Primer 3 were utilized for all hamster samples.

Deep sequencing analysis.

RNA libraries were prepared with 300 ng of RNA using the Click-Seq protocol as previously described [34] using tiled primers cognate to the SARS-COV-2 genome (accession number NC_045512.2) and the TruSeq i7 LT adapter series and i5 hexamer adaptors containing a 12N unique molecular identifier (UMI). Libraries were sequenced on the Illumina MiSeq platform with MiSeq Reagent Kit v2. Raw data was de-multiplexed using TruSeq indexes using the MiSeq Reporter Software. Fastp v0.12. [35] was used to trim adapter sequences and low-quality reads (q<25), remove reads less than 40 nts in length, and copy UMI sequences onto the read name. Reads were aligned with bowtie using the -best parameter and allowing for up to two mismatches. The alignment index was generated from a single fasta file, which contained two 600nt reference sequences spanning the PRRA locus (23603–23616) of the wildtype (accession number NC_045512.2) and ΔPRRA genomes. The alignments were sorted and indexed using Samtools v1.9 [36], PCR duplicates were removed using umi_tools [37]. Coverage at each position was determined with the genomecov function in bedtools v2.25.0 [38].

Plaque reduction neutralization test.

Neutralization assays were preformed using mNeonGreen SARS-CoV-2 reporter neutralization assay as previously described [23]. Briefly, Vero E6 cells were plated black

μCLEAR flat-bottom 96-well plate (Greiner Bio-one™). On following day, sera or monoclonal antibodies were serially diluted from 1/20 with nine 2-fold dilutions to the final dilution of 1/5120 and incubated with mNeonGreen SARS-CoV-2 or ΔPRRA expressing mNeonGreen at 37°C for 1 h. The virus-serum mixture was transferred to the Vero E6 cell plate with a final MOI of 0.5. After 20 h, Hoechst 33342 Solution (400-fold diluted in Hank's Balanced Salt Solution; Gibco) was added to stain cell nucleus, sealed with Breath-Easy sealing membrane (Diversified Biotech), incubated at 37°C for 20 min, and quantified for mNeonGreen fluorescence on Cytation™ 7 (BioTek). The raw images (2×2 montage) were acquired using 4× objective, processed, and stitched using the default setting. The total cells (indicated by nucleus staining) and mNeonGreen-positive cells were quantified for each well. Infection rates were determined by dividing the mNeonGreen-positive cell number to total cell number. Relative infection rates were obtained by normalizing the infection rates of serum-treated groups to those of non-serum-treated controls. The curves of the relative infection rates versus the serum dilutions ($\log_{10}$ values) were plotted using Prism 8 (GraphPad). A nonlinear regression method was used to determine the dilution fold that neutralized 50% of mNeonGreen fluorescence (NT50). Each serum was tested in duplicates.

Phylogenetic tree, sequence identity heat map, and structural modeling.

Heat maps were constructed from a set of representative group 2B coronaviruses by using alignment data paired with neighbor-joining phylogenetic trees built in Geneious (v.9.1.5) using the spike amino acid sequences derived the following accession numbers: QHU79204 (SARS-CoV-2 WA1), QHR63300.2 (RATG13), QND76034.1 (HKU3), AGZ48828.1 (WIV1), AGZ48806 (RsSHC014), ALK02457 (WIV16), and AYV99817.1(SARS-CoV Urbani). Sequence identity was visualized using EvolView (http://evolgenius.info/) and SARS-CoV Co-V-2 WA1 served as the reference sequence. Structural models were generated using SWISS-Model [39,40] to generate homology models for SARS-CoV-2 spike with and without the furin cleavage site based on the SARS-CoV-1 trimer structure (PDB 6ACD). Homology models were visualized and manipulated in MacPyMol (version 1.3).

Transmission Electron Microscopy (TEM).

Supernatants of SARS-CoV-2 infected cells were centrifuged for 10 min at 3,000 g to remove large cellular debris. Nickel grids were incubated with clarified supernatants for 10 min followed by glutaraldehyde fixation and 2% uranyl acetate staining. Micrographs were taken using a JEM 14000 (JEOL USA Inc.). Multiple randomly selected fields were imaged to obtain unbiased particle counts.

Hamster infection studies.

Male Syrian hamsters (7–8 weeks old, 86–127 g) were purchased from Envigo. All procedures were conducted under an animal protocol approved by the UTMB Institutional Animal Care and Use Committee and complied with USDA guidelines in an AAALAC-accredited lab. Work with infectious SARS-CoV-2 in hamsters was performed in the Galveston National Laboratory BSL-4 laboratory. Animals were housed in microisolator caging equipped with HEPA filters in the BSL-4 laboratories. Hamsters were challenged with 10^5 PFU of WT-SARS-CoV-2 or SARS-CoV-2 ΔPRRA by intranasal inoculation (i.n.). Hamsters were observed daily for the development of clinical disease and body weights

were taken every day for the first 10 days of the study, then every third day. For each manipulation (viral infection, retro-orbital bleeds, nasal wash, or oral swab), animals were anesthetized with isoflurane (Piramal, Bethlehem, PA).

Mouse infection studies.

Mouse studies were carried out in accordance with the recommendations in the Guide for the Care and Use of Laboratory Animals of the National Institutes of Health. The protocols were approved by the Institutional Animal Care and Use Committee at the Washington University School of Medicine (assurance number A3381–01) and performed in an ABSL3 facility. Heterozygous K18-hACE C57BL/6J mice (strain: 2B6.Cg-Tg(K18-ACE2)2Prlmn/J) were obtained from The Jackson Laboratory and randomized to upon arrival. Animals were housed in 7.5×11.5×5” cages in groups of ≤5 and fed standard chow diets (PicoLab Rodent Diet 5053, Purina). Cages were changed weekly. The ABSL-3 room was kept between 68–74 degrees Farenheit with 30–60% and 12h-12h light cycles (6AM-6PM). Mice of both sexes were used for experimentation. Animals were housed in groups of ≤5 individuals in rooms maintained between 20.0–23.3oC with 30–60% humidity. Mice were given *ad libitum* access to water and PicoLab Rodent Diet 5053 chow (Purina). Virus inoculations were performed under anesthesia that was induced and maintained with ketamine hydrochloride and xylazine; all efforts were made to minimize animal suffering. Mice of different ages (5–9 weeks old) and both sexes were administered 10^3 PFU of SARS-CoV-2 in a 50 μL intranasal dose.

Cytokine and chemokine protein measurements.

Lung homogenates were incubated with Triton-X-100 (1% final concentration) for 1 h at room temperature to inactivate SARS-CoV-2. Homogenates then were analyzed for cytokines and chemokines by Eve Technologies Corporation (Calgary, AB, Canada) using their Mouse Cytokine Array / Chemokine Array 31-Plex (MD31) platform.

Respiratory mechanics.

Mice were anesthetized with ketamine/xylazine (100 mg/kg and 10 mg/kg, i.p., respectively). The trachea was isolated via dissection of the neck area and cannulated using an 18-gauge blunt metal cannula (typical resistance of 0.18 $cmH_2O.s/mL$), which was secured in place with a nylon suture. The mouse then was connected to the flexiVent computer-controlled piston ventilator (SCIREQ Inc.) via the cannula, which was attached to the FX adaptor Y-tubing. Mechanical ventilation was initiated, and mice were given an additional 100 mg/kg of ketamine and 0.1 mg/mouse of the paralytic pancuronium bromide via intraperitoneal route to prevent breathing efforts against the ventilator and during measurements. Mice were ventilated using default settings for mice, which consisted in a positive end expiratory pressure at 3 cm H2O, a 10 mL/kg tidal volume (Vt), a respiratory rate of 150 breaths per minute (bpm), and a fraction of inspired oxygen (FiO2) of 0.21 (i.e., room air). Respiratory mechanics were assessed using the forced oscillation technique, as previously described [41], using the latest version of the FlexiVent operating software (FlexiWare v8.1.3). Pressure-volume loops and measurements of inspiratory capacity were also performed.

Measurement of viral burden.

Mouse tissues were weighed and homogenized with zirconia beads in a MagNA Lyser instrument (Roche Life Science) in 1000 μL of DMEM media supplemented with 2% heat-inactivated FBS. Tissue homogenates were clarified by centrifugation at 10,000 rpm for 3 min and RNA was extracted from 50uL of supernatant using the MagMax mirVana Total RNA isolation kit (Thermo Scientific) on the Kingfisher Flex extraction robot (Thermo Scientific). RNA was reverse transcribed and amplified using the TaqMan RNA-to-CT 1-Step Kit (ThermoFisher). Reverse transcription was carried out at 48°C for 15 min followed by 2 min at 95°C. Amplification was accomplished over 50 cycles as follows: 95°C for 15 s and 60°C for 1 min. Copies of SARS-CoV-2 N gene RNA in samples were determined using a previously published assay. Briefly, a TaqMan assay was designed to target a highly conserved region of the N gene (Forward primer: ATGCTGCAATCGTGCTACAA; Reverse primer: GACTGCCGCCTCTGCTC; Probe: /56-FAM/TCAAGGAAC/ZEN/ AACATTGCCAA/3IABkFQ/). This region was included in an RNA standard to allow for copy number determination down to 10 copies per reaction. The reaction mixture contained final concentrations of primers and probe of 500 and 100 nM, respectively.

Histology and RNA in situ hybridization.

Upon euthanasia, the lung was inflated with ~1.2 mL of 10% neutral buffered formalin using a 3-mL syringe and catheter inserted into the trachea. The airway, lungs, and heart were removed en bloc and transferred to a conical containing 40 mL 10% neutral buffered formalin, where the tissues were allowed to fix for suspension of neutral buffered formalin for ≥7 days. Tissues were embedded in paraffin, and sections were stained with hematoxylin and eosin by the Washington University Lung Morphology Core. Images were captured using the Nanozoomer (Hamamatsu) at the Alafi Neuroimaging Core at Washington University.

Data Availability.

The raw data that support the findings of this study are available from the corresponding author upon reasonable request.[42]

Biological Materials.

Recombinant wild-type and mutant SARS-CoV-2 described in this manuscript will be made available through the World Reference Center for Emerging Viruses and Arboviruses (WRCEVA) at UTMB through material transfer agreement.

Extended Data

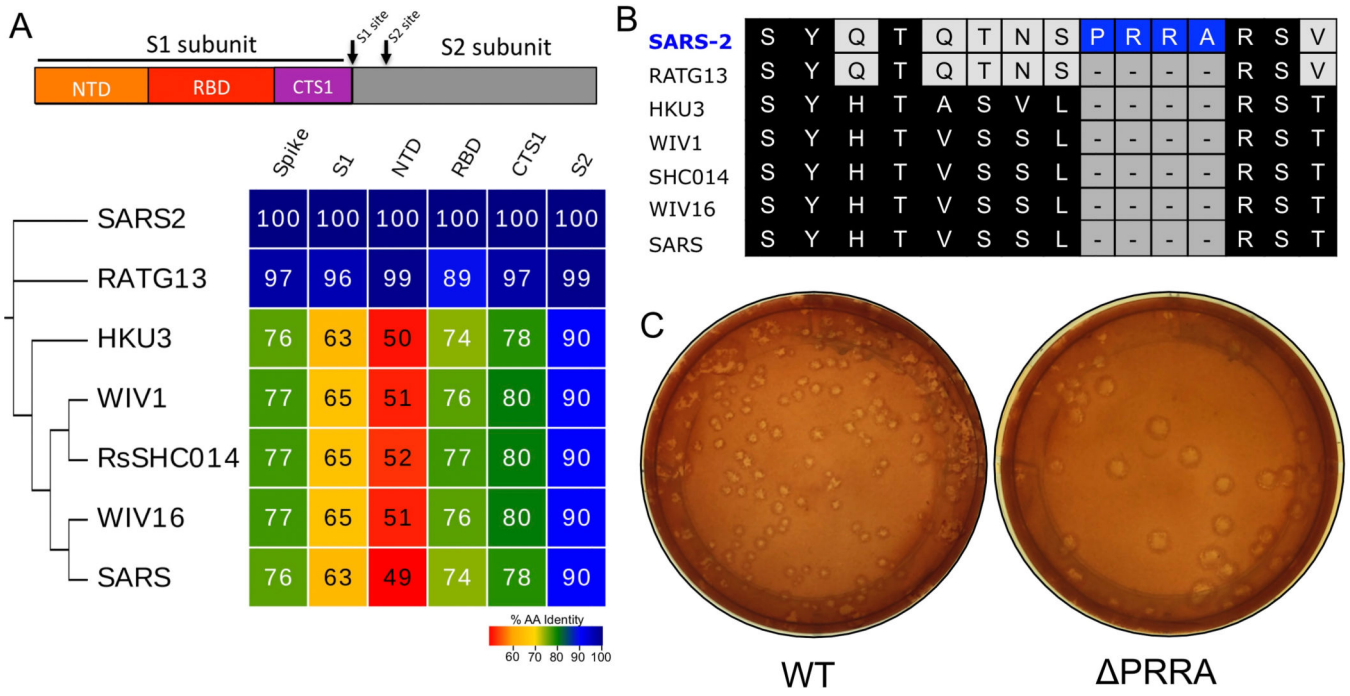

Extended Data Figure 1. Furin cleavage site in SARS-CoV-2 spike.

A) Diagram of the coronavirus spike protein domains and cleavage sites. The sequences of the indicated group 2B coronaviruses were aligned according to the bounds of total spike, S1, N-terminal domain (NTD), Receptor binding domain (RBD), and C-terminal of S1 (CTS1) and S2. Sequence identities were extracted from the alignments, and a heatmap of sequence identity was constructed using EvolView (www.evolgenius.info/evolview) with SARS-CoV-2 WA1 as the reference sequence. B) Alignment of the furin cleavage site of SARS-CoV-2 and the corresponding amino acids identities found closely related group 2B CoVs. The PRRA insertion is unique to SARS-CoV-2 C) Representative plaque morphology of WT and ΔPRRA SARS-CoV-2.

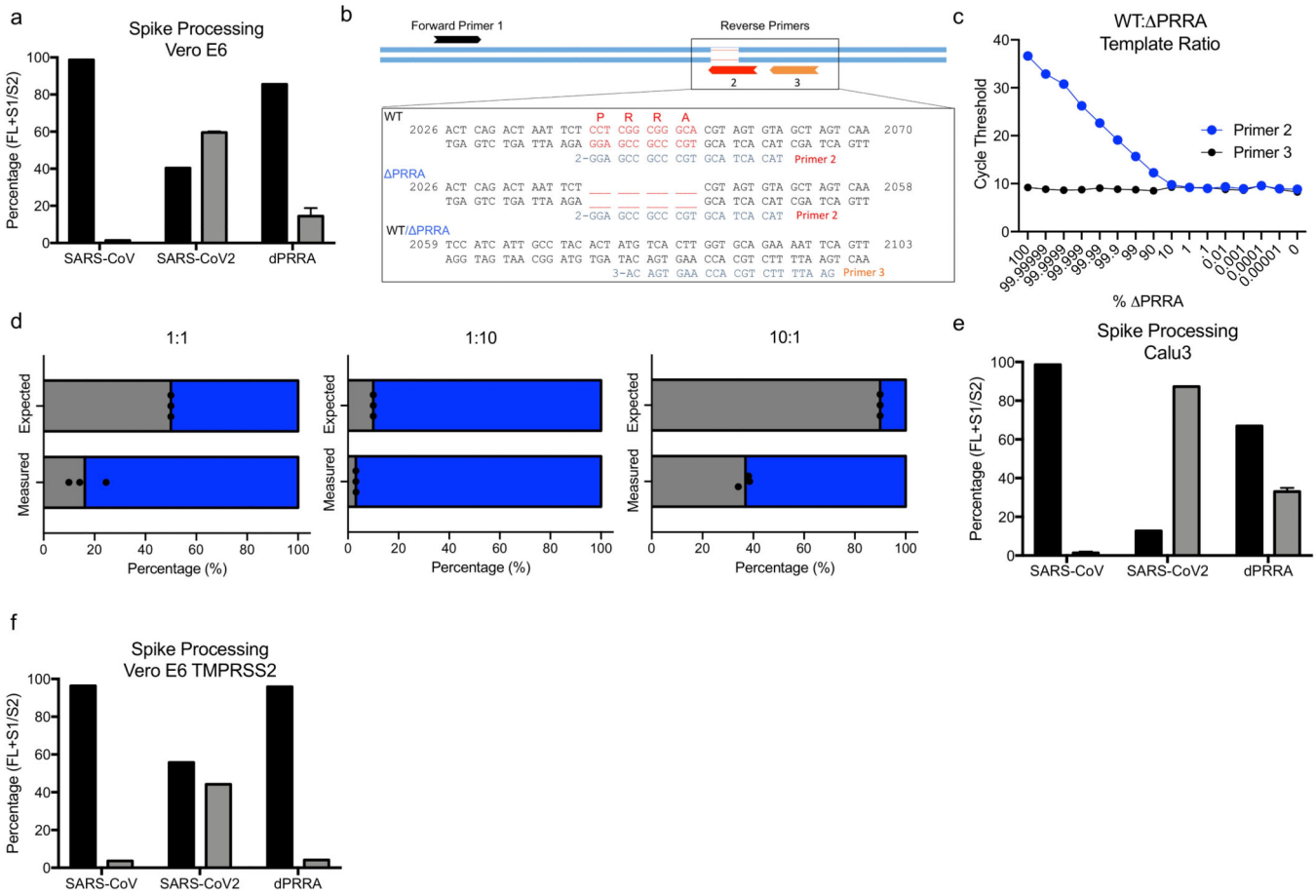

Extended Data Figure 2. ΔPRRA mutant processing and competition with WT.

A) Quantitation by densitometry of the full-length spike (Black) and S1/S2 cleavage form (Gray) from distinct western blot experiments in Vero E6 cells (n=2). B) Schematic of quantitative RT-PCR approach to detect deletion of the furin cleavage site. C) Primer curve validation with mixed WT to ΔPRRA plasmid ratio showing sensitivity. D) Deep sequencing results from ΔPRRA and WT competition assays based on percentage of total reads in that region (N=3). E) Quantitation by densitometry of the full-length spike (Black) and S1/S2 cleavage form (Gray) from distinct western blot experiments from Calu3 (n=2). F) Quantitation by densitometry of the full-length spike (Black) and S1/S2 cleavage form (Gray) from distinct western blot experiments from Vero E6 cell expressing *TMPRSS2* (n=2). Data are presented as mean values.

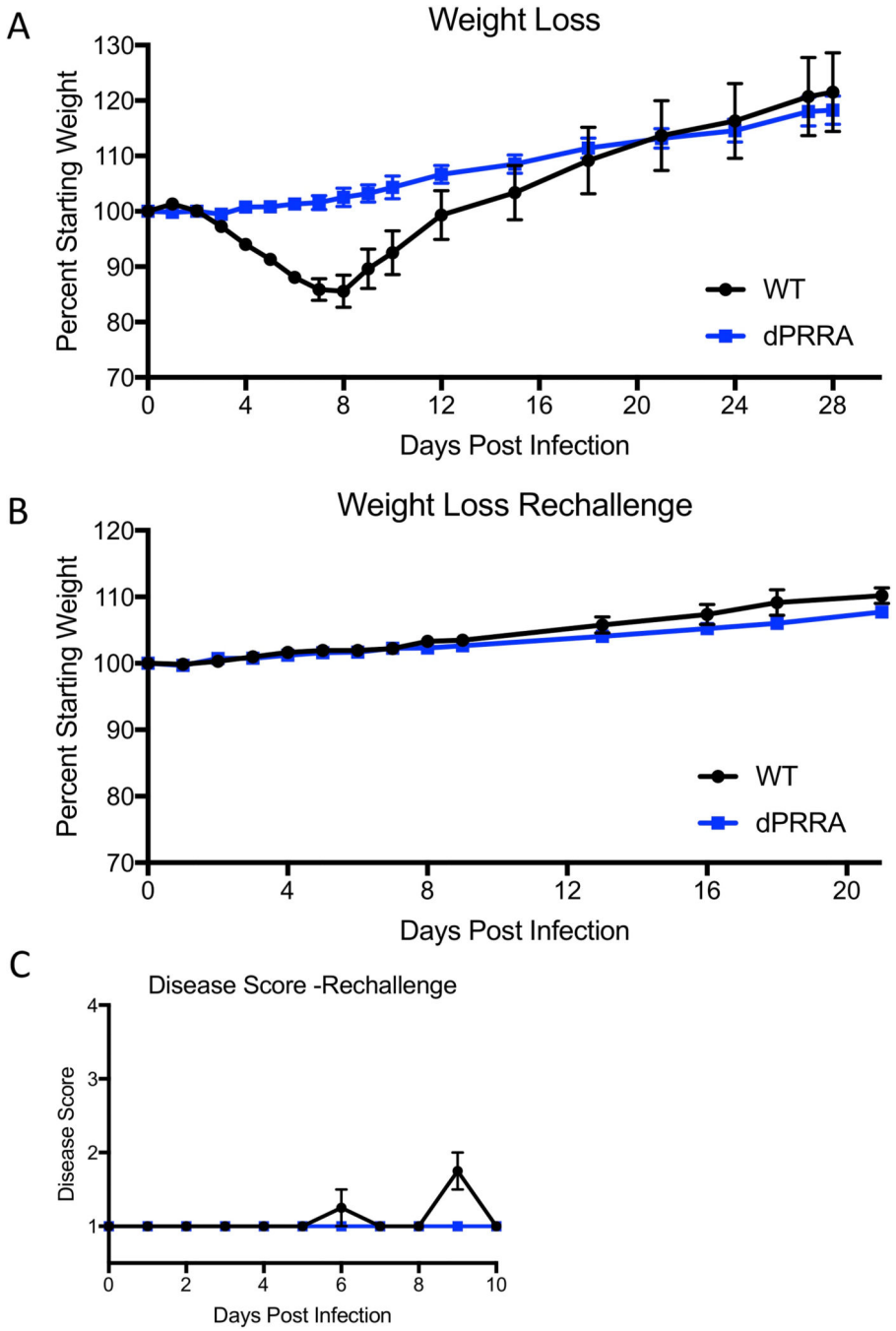

Extended Data Figure 3. ***In vivo*** **attenuation of ΔPRRA mutant.**

a) Weight loss following primary WT and ΔPRRA mutant SARS-CoV-2 challenge (N=4 per group). **b & c**)Weight loss (**b**) and disease score (**c**) following rechallenge of WT and ΔPRRA mutant infected mice with WT SARS-CoV-2 (N=4 per group). Data are presented as mean values +/−SEM.

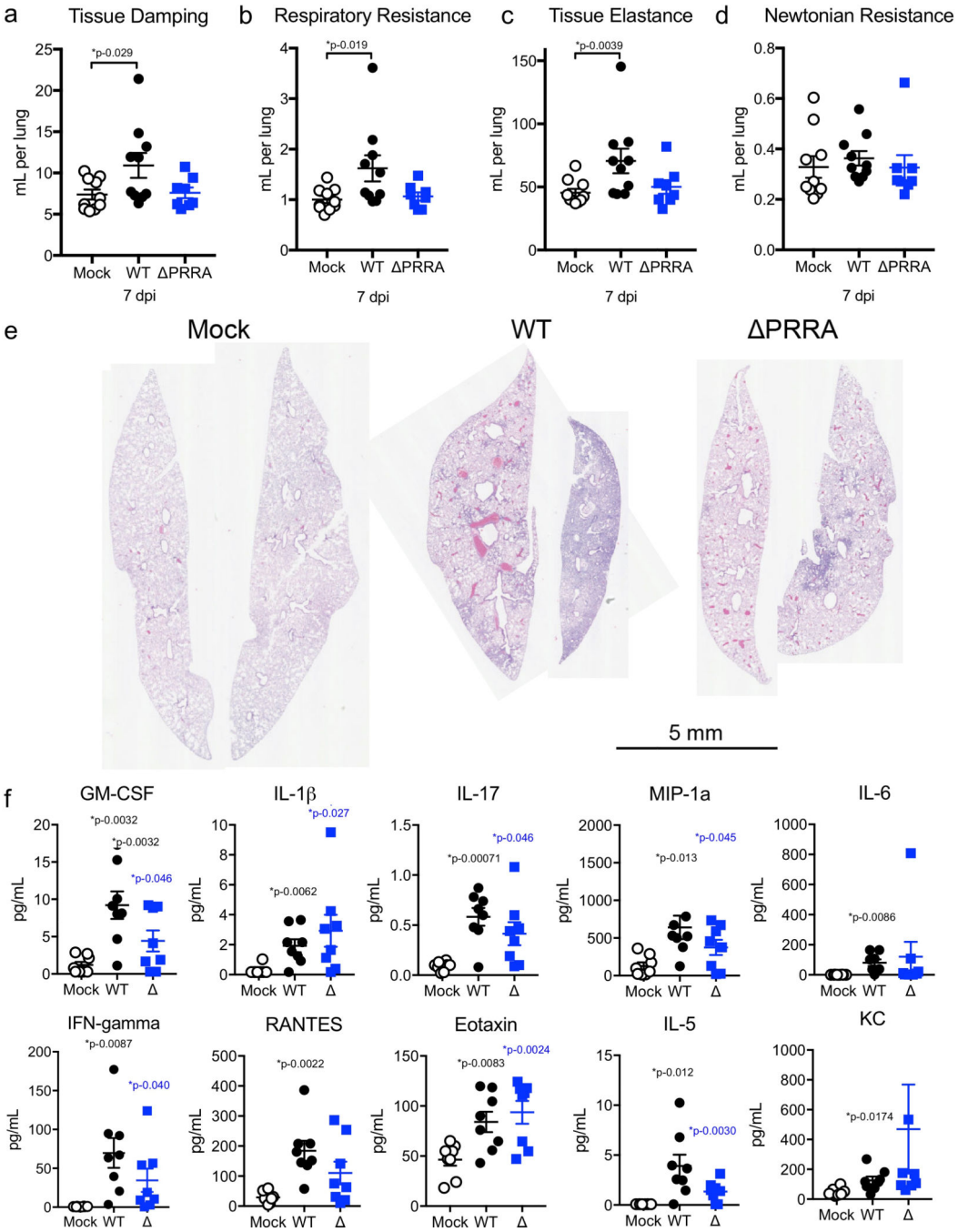

Extended Data Figure 4. ***In vivo*** **attenuation of ΔPRRA mutant in K18-hACE2 mice.**

a-d) Lung function evaluated using flexivent for a) tissue damping, b) respiratory resistance c) tissue elastance, and d) Newtonian resistance. (a-d) N= 10 for WT and 8 for ΔPRRA. E) Whole lung histopathology sections seven days post infection from I) mock, J) WT and K) dPRRA infected mice with least (left) and most (right) severe sections as representative samples from 3 mock, 2 WT, and 3 ΔPRRA infected mice F) Chemokine/cytokine analysis of mouse lung seven days post infection with mock (open), WT (black), or ΔPRRA SARS-CoV-2. N=8 for all groups. P-values based on a two-tailed Mann-Whitney (**a-d**) or a two-

tailed student T-test (**f**) relative to control. Data are presented as mean values +/−SEM. Scale bar represents 5mm.

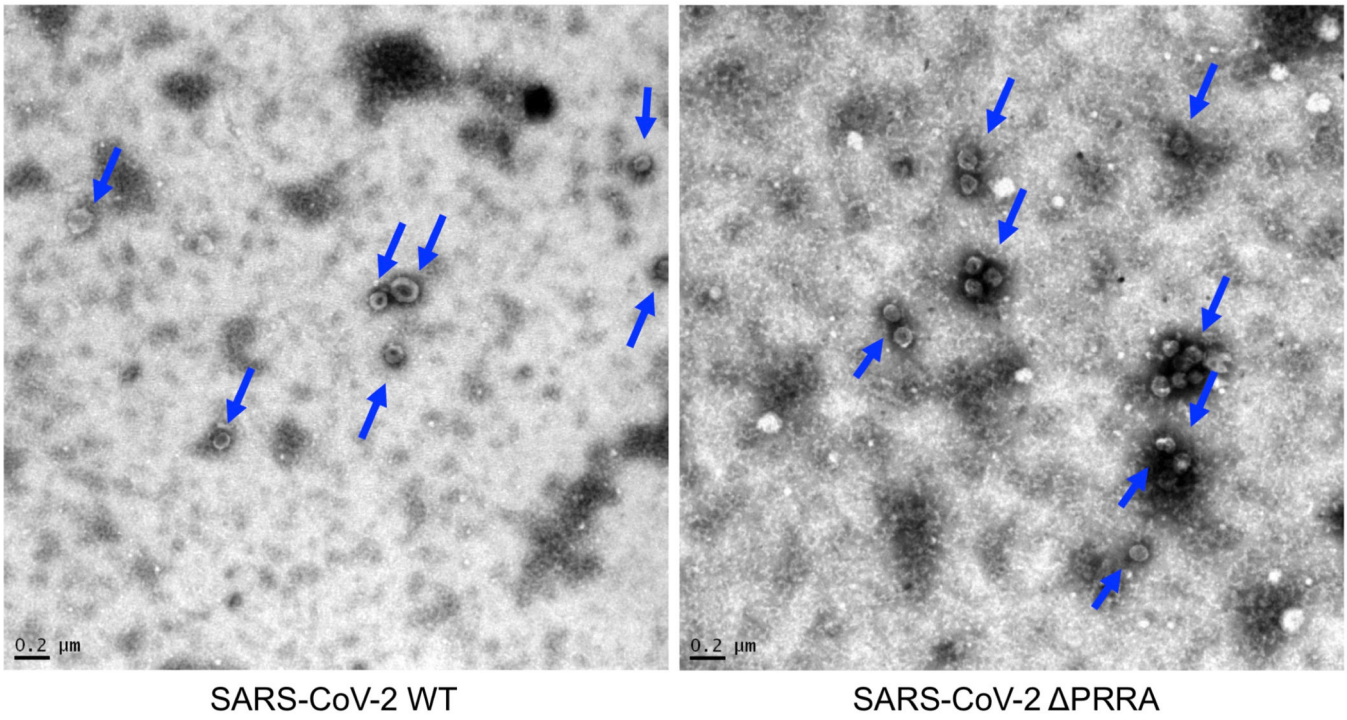

Extended Data Figure 5. ΔPRRA Virion Morphology and Clumping.
Transmission electron microscopy of WT (left) and ΔPRRA (right) SARS-CoV-2 with arrows signifying individual virion particles. Images representative of two preparations and 40 individual images observed for WT and ΔPRRA mutant. Scale bar represents 0.2 µm.

Extended Data Table 1.
Statistical significance of antibody conditions based on EC50 values.

EC50 values reflect the curve fit determined by the pooled data of all three replicates per virus/antibody composition. P-values reflect unpaired, two-tailed t-test of the values derived from curves fit to each individual replicate. Correction for multiple (6) comparisons utilizes the Holm-Sidak method.

Antibody	EC50 Value	P-Value
COVID Sera – High	0.0004632	0.000468
COVID Sera – Intermediate	0.001070	0.006592
COVID Sera – Low	0.01024	0.154211
mAB1	0.299	0.006592
mAB2	0.9203	0.154211
mAB3	0.6571	0.001259

Supplementary Material

Refer to Web version on PubMed Central for supplementary material.

Acknowledgements.

Research was supported by grants from NIA and NIAID of the NIH to (AI153602 and AG049042 to VDM AI142759, AI134907, AI145617, and UL1TR001439 to P-YS; R01AI123449 to AF and BL; R24AI120942 (WRCEVA) to SCW, R01AI157155 and Defense Advanced Research Project Agency (HR001117S0019) to MSD). Research was also supported by STARs Award provided by the University of Texas System to VDM and trainee funding provided by the McLaughlin Fellowship Fund at UTMB. P-YS was also supported by CDC grant for the Western Gulf Center of Excellence for Vector-Borne Diseases, and awards from the Sealy & Smith Foundation, Kleberg Foundation, John S. Dunn Foundation, Amon G. Carter Foundation, Gilson Longenbaugh Foundation, and Summerfield Robert Foundation.

References

1. Gralinski LE & Menachery VD Return of the Coronavirus: 2019-nCoV. Viruses 12(2020).
2. Coutard B, et al. The spike glycoprotein of the new coronavirus 2019-nCoV contains a furin-like cleavage site absent in CoV of the same clade. Antiviral Res 176, 104742 (2020).
3. Dong E, Du H & Gardner L An interactive web-based dashboard to track COVID-19 in real time. Lancet Infect Dis 20, 533–534 (2020). [PubMed: 32087114]
4. Huang C, et al. Clinical features of patients infected with 2019 novel coronavirus in Wuhan, China. Lancet 395, 497–506 (2020). [PubMed: 31986264]
5. Gao Z, et al. A Systematic Review of Asymptomatic Infections with COVID-19. J Microbiol Immunol Infect (2020).
6. Shang J, et al. Structural basis of receptor recognition by SARS-CoV-2. Nature 581, 221–224 (2020). [PubMed: 32225175]
7. Seidah NG & Chretien M Proprotein and prohormone convertases: a family of subtilases generating diverse bioactive polypeptides. Brain Res 848, 45–62 (1999). [PubMed: 10701998]
8. Wrobel AG, et al. SARS-CoV-2 and bat RaTG13 spike glycoprotein structures inform on virus evolution and furin-cleavage effects. Nature structural & molecular biology 27, 763–767 (2020).
9. Hoffmann M, Kleine-Weber H & Pöhlmann S A Multibasic Cleavage Site in the Spike Protein of SARS-CoV-2 Is Essential for Infection of Human Lung Cells. Mol Cell 78, 779–784.e775 (2020).
10. Bestle D, et al. TMPRSS2 and furin are both essential for proteolytic activation of SARS-CoV-2 in human airway cells. Life science alliance 3(2020).
11. Lau SY, et al. Attenuated SARS-CoV-2 variants with deletions at the S1/S2 junction. Emerging microbes & infections 9, 837–842 (2020). [PubMed: 32301390]
12. Klimstra WB, et al. SARS-CoV-2 growth, furin-cleavage-site adaptation and neutralization using serum from acutely infected hospitalized COVID-19 patients. J Gen Virol (2020).
13. Plante JA, et al. Spike mutation D614G alters SARS-CoV-2 fitness. Nature (2020).
14. Zhang L, et al. The D614G mutation in the SARS-CoV-2 spike protein reduces S1 shedding and increases infectivity. bioRxiv (2020).
15. Xie X, et al. An Infectious cDNA Clone of SARS-CoV-2. Cell host & microbe 27, 841–848 e843 (2020).
16. Harcourt J, et al. Severe Acute Respiratory Syndrome Coronavirus 2 from Patient with 2019 Novel Coronavirus Disease, United States. Emerg Infect Dis 26(2020).
17. Menachery VD, et al. Pathogenic influenza viruses and coronaviruses utilize similar and contrasting approaches to control interferon-stimulated gene responses. mBio 5, e01174–01114 (2014).
18. Matsuyama S, et al. Enhanced isolation of SARS-CoV-2 by TMPRSS2-expressing cells. Proceedings of the National Academy of Sciences of the United States of America 117, 7001–7003 (2020). [PubMed: 32165541]

19. Imai M, et al. Syrian hamsters as a small animal model for SARS-CoV-2 infection and countermeasure development. Proceedings of the National Academy of Sciences of the United States of America 117, 16587–16595 (2020).
20. Tostanoski LH, et al. Ad26 vaccine protects against SARS-CoV-2 severe clinical disease in hamsters. Nature medicine (2020).
21. Bos R, et al. Ad26 vector-based COVID-19 vaccine encoding a prefusion-stabilized SARS-CoV-2 Spike immunogen induces potent humoral and cellular immune responses. npj Vaccines 5, 91 (2020). [PubMed: 33083026]
22. Winkler ES, et al. SARS-CoV-2 infection of human ACE2-transgenic mice causes severe lung inflammation and impaired function. Nature immunology 21, 1327–1335 (2020). [PubMed: 32839612]
23. Muruato AE, et al. A high-throughput neutralizing antibody assay for COVID-19 diagnosis and vaccine evaluation. Nature communications 11, 4059 (2020).
24. Santiana M, et al. Vesicle-Cloaked Virus Clusters Are Optimal Units for Inter-organismal Viral Transmission. Cell host & microbe 24, 208–220.e208 (2018).
25. Rivera-Serrano EE, González-López O, Das A & Lemon SM Cellular entry and uncoating of naked and quasi-enveloped human hepatoviruses. eLife 8(2019).
26. Gao Q, et al. Development of an inactivated vaccine candidate for SARS-CoV-2. Science 369, 77–81 (2020). [PubMed: 32376603]
27. Hansen J, et al. Studies in humanized mice and convalescent humans yield a SARS-CoV-2 antibody cocktail. Science (2020).

Methods References

28. Harcourt J, et al. Severe Acute Respiratory Syndrome Coronavirus 2 from Patient with 2019 Novel Coronavirus Disease, United States. Emerg Infect Dis 26(2020).
29. Roberts A, et al. A mouse-adapted SARS-coronavirus causes disease and mortality in BALB/c mice. PLoS pathogens 3, e5 (2007).
30. Sims AC, et al. Release of severe acute respiratory syndrome coronavirus nuclear import block enhances host transcription in human lung cells. J Virol 87, 3885–3902 (2013). [PubMed: 23365422]
31. Josset L, et al. Cell host response to infection with novel human coronavirus EMC predicts potential antivirals and important differences with SARS coronavirus. MBio 4, e00165–00113 (2013).
32. Xie X, et al. An Infectious cDNA Clone of SARS-CoV-2. Cell host & microbe 27, 841–848 e843 (2020).
33. Sheahan T, Rockx B, Donaldson E, Corti D & Baric R Pathways of cross-species transmission of synthetically reconstructed zoonotic severe acute respiratory syndrome coronavirus. Journal of virology 82, 8721–8732 (2008). [PubMed: 18579604]
34. Menachery VD, et al. Attenuation and restoration of severe acute respiratory syndrome coronavirus mutant lacking 2'-o-methyltransferase activity. Journal of virology 88, 4251–4264 (2014). [PubMed: 24478444]
35. van Tol S, et al. VAMP8 Contributes to the TRIM6-Mediated Type I Interferon Antiviral Response during West Nile Virus Infection. Journal of virology 94(2020).
36. Routh A, Head SR, Ordoukhanian P & Johnson JE ClickSeq: Fragmentation-Free Next-Generation Sequencing via Click Ligation of Adaptors to Stochastically Terminated 3'-Azido cDNAs. J Mol Biol 427, 2610–2616 (2015). [PubMed: 26116762]
37. Chen S, Zhou Y, Chen Y & Gu J fastp: an ultra-fast all-in-one FASTQ preprocessor. Bioinformatics 34, i884–i890 (2018). [PubMed: 30423086]
38. Li H, et al. The Sequence Alignment/Map format and SAMtools. Bioinformatics 25, 2078–2079 (2009). [PubMed: 19505943]
39. Smith T, Heger A & Sudbery I UMI-tools: modeling sequencing errors in Unique Molecular Identifiers to improve quantification accuracy. Genome Res 27, 491–499 (2017). [PubMed: 28100584]

40. Quinlan AR & Hall IM BEDTools: a flexible suite of utilities for comparing genomic features. Bioinformatics 26, 841–842 (2010). [PubMed: 20110278]

41. Muruato AE, et al. A high-throughput neutralizing antibody assay for COVID-19 diagnosis and vaccine evaluation. Nature communications 11, 4059 (2020).

42. Waterhouse A, et al. SWISS-MODEL: homology modelling of protein structures and complexes. Nucleic Acids Res 46, W296–W303 (2018). [PubMed: 29788355]

43. Bienert S, et al. The SWISS-MODEL Repository-new features and functionality. Nucleic Acids Res 45, D313–D319 (2017). [PubMed: 27899672]

44. McGovern TK, Robichaud A, Fereydoonzad L, Schuessler TF & Martin JG Evaluation of respiratory system mechanics in mice using the forced oscillation technique. J Vis Exp, e50172 (2013).

45. Gralinski LE, et al. Mechanisms of Severe Acute Respiratory Syndrome Coronavirus-Induced Acute Lung Injury. mBio 4(2013).

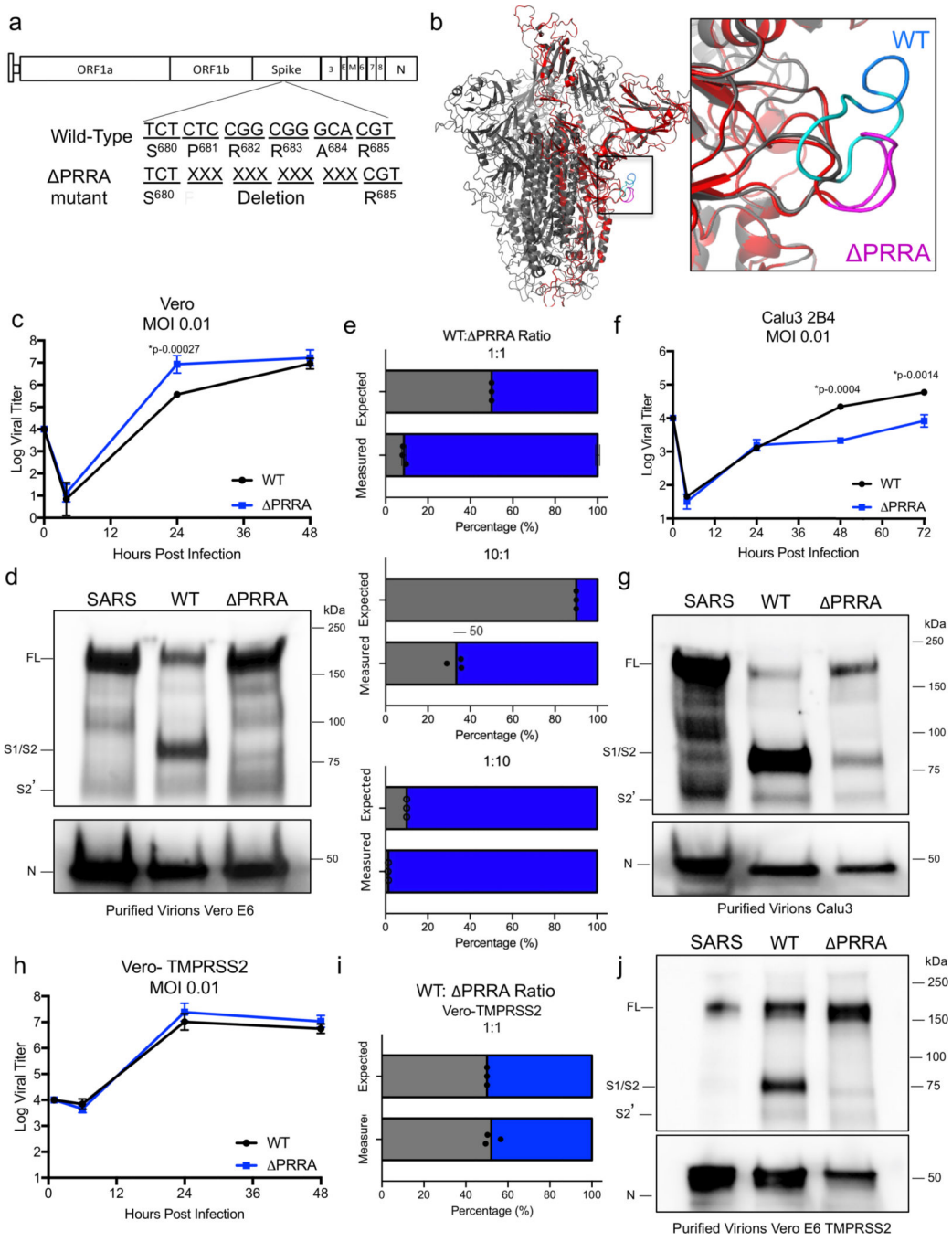

Figure 1. Distinct replication, spike cleavage, and competition for ΔPRRA.

a) SARS-CoV-2 schematic to delete the furin cleavage site. b) SARS-CoV-2 trimer (grey) with PRRA deletion mutant monomer overlaid (red). The loop (inset) shows WT SARS-CoV-2 (cyan) with the PRRA sequence (blue) and PRRA deletion mutant (pink). Models were generated using SARS-CoV structure (PDB 6ACD). c) Viral titer from Vero E6 cells infected with WT SARS-CoV-2 (black) or ΔPRRA (blue) at MOI 0.01 (N=3). d) Purified SARS-CoV, SARS-CoV-2 WT, and ΔPRRA virions from Vero E6 cells probed with anti-spike (Top panel) or anti-nucleocapsid antibody (lower panel). Full length (FL), S1/S2

cleavage form, and S2’ annotated. Results representative of two independent experiments. e) Competition assay between SARS-CoV-2 WT (black) and ΔPRRA (blue) showing RNA percentage based on quantitative RT-PCR at 50:50, 90:10, and 10:90 WT/ΔPRRA ratio (N=3 per group). f) Viral titer from Calu3 2B4 cells infected with WT SARS-CoV-2 (black) or ΔPRRA (blue) at MOI 0.01 (N=3). g) Purified SARS-CoV, SARS-CoV-2 WT, and ΔPRRA virions from Calu3 2B4 cells probed with anti-spike (top panel) or anti-nucleocapsid antibody (lower panel). Results representative of two independent experiments. h) Viral titer from Vero E6 cells expressing TMPRSS2 infected with WT SARS-CoV-2 (black) or ΔPRRA (blue) at MOI 0.01 (N=5). i) Competition assay between SARS-CoV-2 WT (black) and ΔPRRA (blue) on Vero E6 cells expressing TMPRSS2 showing RNA percentage based on quantitative RT-PCR at 50:50 WT/ΔPRRA ratio (N=3 per group). j) Purified SARS-CoV, SARS-CoV-2 WT, and ΔPRRA virions from Vero E6 cells expressing TMPRSS2 probed with anti-spike (Top) or anti-nucleocapsid antibody (lower). Results representative of two independent experiments. Data presented as mean values +/− SD in c, e, f, h and i. P-values based on a two-tailed Student T-test.

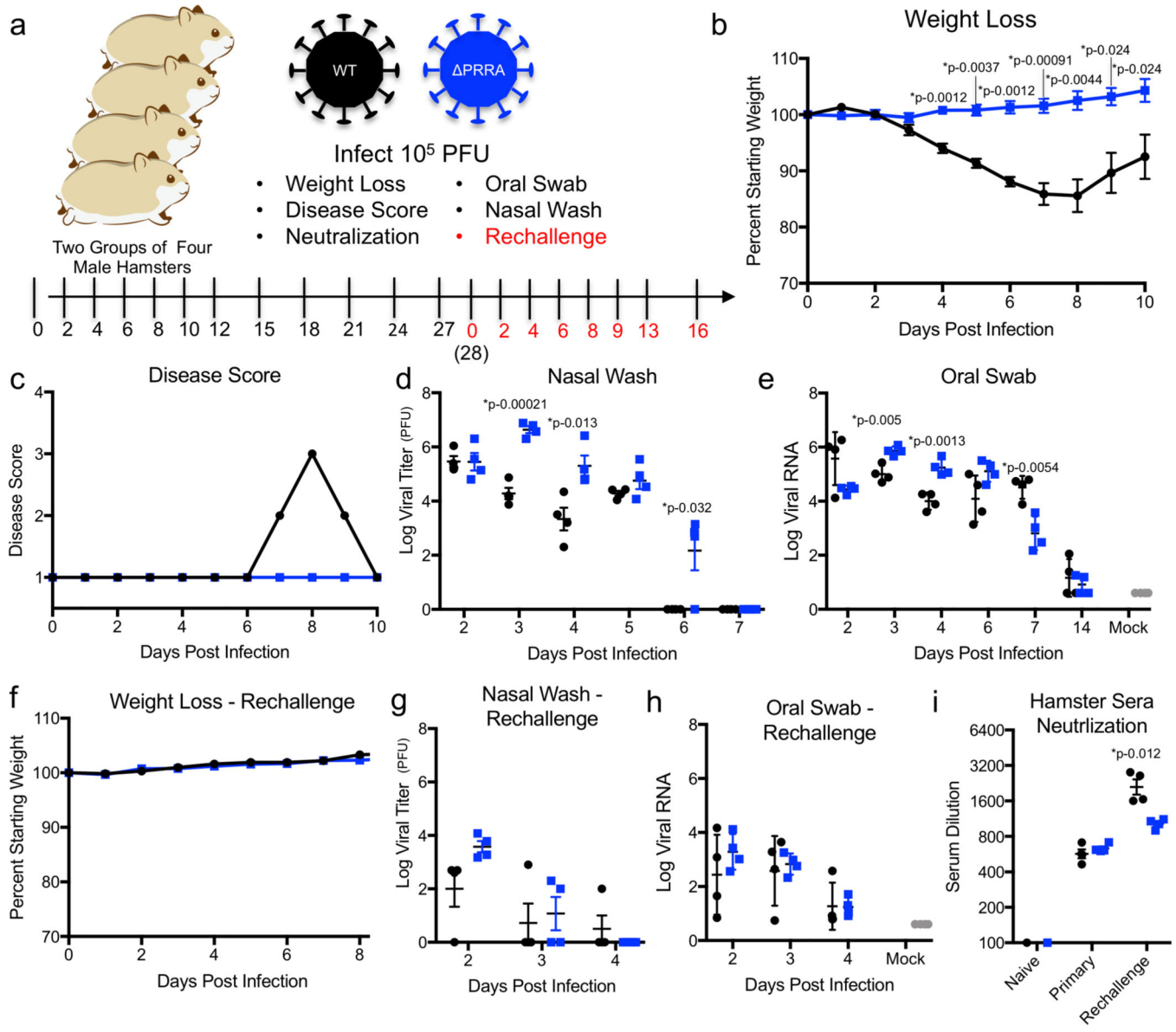

Figure 2. Hamster infections with ΔPRRA mutant.

a, Primary SARS-CoV-2 challenge schematic. Two groups of male hamsters (N=4) were challenged with 10^5 plaque forming units (PFU) of either SARS-CoV-2 WT or ΔPRRA mutant and evaluated (b) weight loss, (c) disease score, (d) viral titer from nasal wash and (e) viral RNA from oral swabs. f-k, Twenty eight DPI, hamsters infected with SARS-CoV-2 WT or ΔPRRA were rechallenged with 10^5 PFU of SARS-CoV-2 WT and evaluated for (f) weight loss, (g) viral titer from nasal wash, (h) viral RNA from oral swabs, and (i) PRNT50 dilution from primary and rechallenge hamster sera. Data presented as mean values +/− SEM. P-values based on a two-tailed Student T-test.

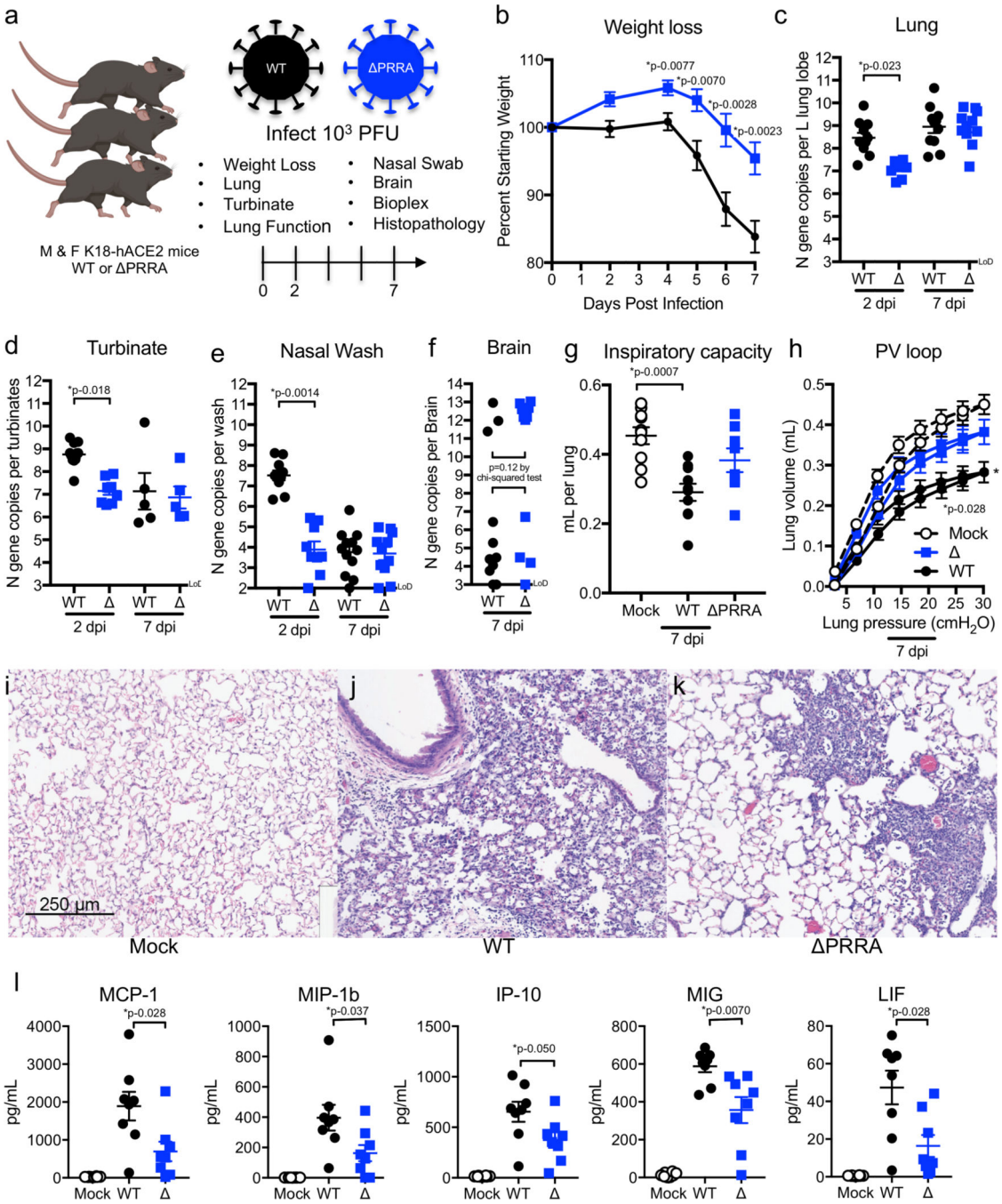

Figure 3. Infection of K18-hACE2 transgenic mice with ΔPRRA mutant.

a, SARS-CoV-2 challenge schematic created with BioRender. Male and female mice were challenged with 10^3 PFU of SARS-CoV-2 WT (black) or ΔPRRA mutant (blue) and evaluated for (b) weight loss (N=12 for both groups), viral RNA from the (c) lung (d) nasal turbinate, (e) nasal wash, and (f) brain. N=9 for WT and 11 ΔPRRA D2, N=11 for both at D4. g-h, Lung function evaluated using Flexivent mechanical ventilator to assess (g) inspiratory capacity, and (h) pressure/volume (PV) loop. N= 10 for WT and 9 for ΔPRRA. i-k, Lung histopathology 7 DPI from (i) mock, (j) WT and (k) ΔPRRA infected mice. Images

represent lung sections from 3 mock, 3 WT, and 3 of ΔPRRA infected mice. l, Chemokine analysis of mouse lung homogenates at 7 DPI with mock (open), WT (black), or ΔPRRA SARS-CoV-2 (blue). N=8 for all groups. Data are presented as mean values +/− SEM. Scale bar represents 250 μm for (i-k). P-values based on a two-tailed Student T-test with unequal variance (b), Kruskal-Wallis Test for multiple comparisons (c-k) or a two-tailed Mann-Whitney test between WT and ΔPRRA (l).

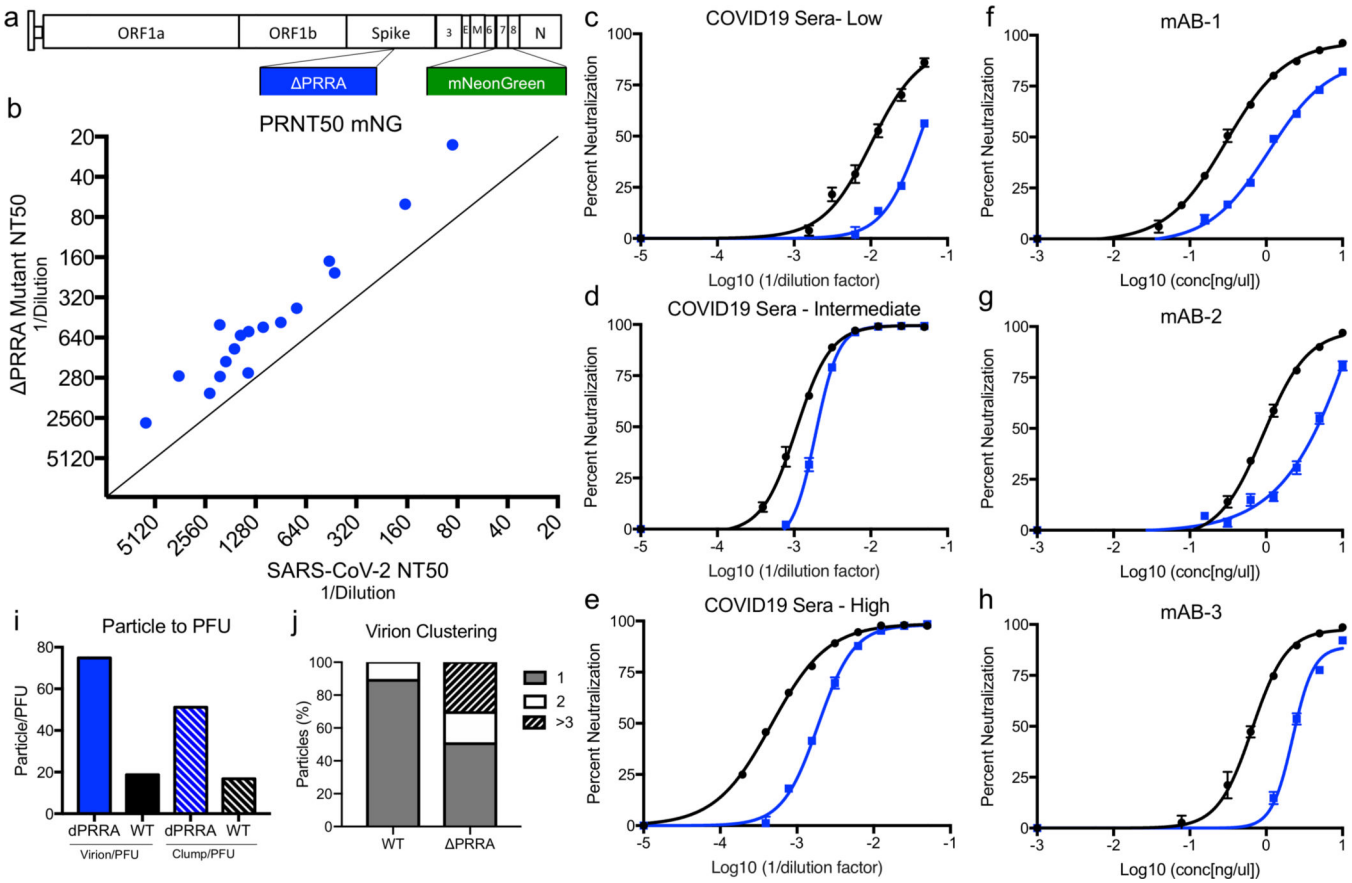

Figure 4. Acessing antibody neutralization of ΔPRRA mutant.

a) Schematic for SARS-CoV-2 ΔPRRA reporter virus expressing mNeonGreen (mNG) gene in place of ORF7. b) Plaque reduction neutralization (PRNT50) values measured mNG expression. PRNT50 values plotted as Log (1/serum dilution) with ΔPRRA on Y axis and WT on the X axis. c-e) Representative curves from c) low, d) intermediate, and e) high neutralizing COVID-19 patient sera. N=3. f-h) Neutralization curves from mAB-1 (f), mAB-2 (g), and mAB-3 (h), N=3. i) Particle/PFU ratio determined from 40 fields dividing into individual particle (left) and clusters to determine ratio. j) Percentage of particles as individual virions (1), doubles (2) or larger clusters (>3). Data are presented as mean values +/− SEM.